Editors' Suggestion

Well-defined metal-polymer nanocomposites: The interplay of structure, thermoplasmonics, and elastic mechanical properties

David Saleta Reig,[1] Patrick Hummel,[2] Zuyuan Wang,[1] Sabine Rosenfeldt,[2,3] Bartlomiej Graczykowski,[1] Markus Retsch,[2,*] and George Fytas[1,4,†]

[1]*Max Planck Institute for Polymer Research, Ackermannweg 10, 55128 Mainz, Germany*

[2]*Department of Chemistry, University of Bayreuth, Universitätsstraße 30, 95447 Bayreuth, Germany*

[3]*Bavarian Polymer Institute, University of Bayreuth, Universitätsstraße 30, 95447 Bayreuth, Germany*

[4]*Departments of Chemistry and Materials Science & Technology, University of Crete and FORTH, P.O. Box 71110, Heraklion, Greece*

(Received 7 August 2018; published 27 December 2018)

Metal-polymer nanocomposites are hybrid materials combining the superior plasmonic, electrical, and thermal properties of metals with the good elasticity and manufacturability of polymers. This renders metal-polymer nanocomposites promising candidates for conductive filler and coating applications, where mechanical properties are optothermally coupled. Here, we study the interplay of nanostructure, thermoplasmonics, and elastic mechanical properties of silver-polystyrene nanocomposites (AgPS) by transmission electron microscopy, small-angle x-ray scattering, Brillouin light scattering (BLS), and other supplemental techniques. We utilize the well-known particle-brush architecture to ensure a homogeneous and isotropic nanoparticle distribution throughout the hybrid material. The effective longitudinal modulus of the as-prepared samples is found to decrease from 5.7 to 4.8 GPa with increasing Ag content from 0 to 4.4 vol.%. Temperature-dependent BLS measurements reveal the unique contribution of local thermoplasmonic heating that depends on the Ag nanoparticle composition. This thermoplasmonic effect results in a lower apparent glass transition temperature (T_g) and a stronger laser power dependence of the speed of sound. Exceeding moderate thermal annealing temperatures ($>150\,^{\circ}$C) leads to a strong structural rearrangement within the homogeneous nanocomposite material with a peculiar clustering-redispersion effect, which also translates into altered mechanical properties. The annealing-induced Ag nanoparticle aggregation results in an even stronger thermoplasmonic effect. We validate our experimental findings with complementary thermographic measurements and finite-element modeling. Overall, this work demonstrates the combined effects of composition and (reversible) aggregation on the mechanical and thermoplasmonic properties of metal-polymer nanocomposites. It not only deepens our understanding of the interaction between light, temperature, and mechanical properties in metal-polymer nanocomposites but also provides a guide for customizing AgPS nanocomposites for potential applications.

DOI: 10.1103/PhysRevMaterials.2.123605

I. INTRODUCTION

Composite materials strive to combine the unique properties of vastly different materials. Classic examples are carbon fiber reinforced polymers, which marry the high mechanical strength of carbon fibers with the low density of polymers. Ideally, the combination of two materials leads to superior properties exceeding the bulk behavior of the constituents owing to a synergistic interplay between the two components. In particular, composite materials at the nanoscale could possess unforeseen effective material properties due to the local confinement of the two components. As a consequence, such materials feature novel structural, mechanical, optical, semiconducting, and thermal properties [1–11].

Nanocomposite materials can be classified concerning their constituting entities, which can comprise any combination of metals, metal oxides, and organic materials, in particular, polymers. Alternatively, the shape of the nanocomposite objects can be used as a distinctive criterion. These include two-dimensional sheets, layers, or stacks, isotropic and anisotropic nanoparticles, and fibers. Most widespread are particulate nanocomposites, comprising a spherical core and a corona. Within this class of nanocomposite materials, polymer shell/rigid core nanoparticles have recently attracted considerable interest [6,12]. The usage of a suitable polymer corona increases the uniformity and stability of the nanoparticle dispersion in a polymer matrix. Still, the nanoconfinement of the polymer corona tethered to a rigid core evokes conformational changes and reduces the entropy, which can result in isotropic or anisotropic aggregates [12]. Only polymer-brush architectures of sufficiently high grafting density yield thermodynamically stable and fully miscible polymer nanocomposites [13]. This brush architecture not only strongly encapsulates the inorganic core but also provides sufficient entropic freedom at the periphery to intimately blend them into the surrounding polymer matrix. The conformation of the "hairy" polymer layer around the rigid core depends on the polymer length and grafting density [14]. In the absence of additional matrix polymers, the grafted polymer corona solely governs the volume fraction and distance of the

*markus.retsch@uni-bayreuth.de

†fytas@mpip-mainz.mpg.de

inorganic core particles. Concomitantly, self-assembled films of such nanocomposite particles represent a homogeneous, one-component material with the polymer-brush nanoparticle architecture as the repetitive motif.

The fabrication of such fully miscible nanocomposite materials poses a particular challenge. Nanoscale objects inherently tend to form aggregates owing to the tendency to reduce the overall surface area and to release adsorbed molecules. Metallic nanoparticles exhibit a particularly large tendency toward clustering, due to their strong, attractive van der Waals interactions. This aggregation trend can be counteracted using specific functional or polymer groups on the particle surface. Grafting-to [13,15] and grafting-from [7] approaches are both suitable to produce densely grafted and stable nanocomposite materials. Hummel *et al.* recently introduced a scalable and reproducible method to synthesize polymer ligand-coated silver nanoparticles with high grafting densities, allowing for a precise adjustment of the interparticle distance [16]. Although the thermodynamical equilibrium structure should be a fcc crystal as for the case of large, densely polymer-tethered dielectric particles [17], the strong, attractive van der Waals forces along with the self-assembly procedure can result in less-ordered nanostructures as well [18].

Whereas many nanocomposite materials base on metal-oxide (most commonly SiO_2) cores [17,19], we want to emphasize the added functionality provided by plasmonic cores. Plasmonic nanocomposites may exhibit cooperative effects such as local plasmonic hotspot or lattice plasmon formation, owing to the small interparticle distance [20]. These can change the effective spectral response and the optical density [21,22]. Furthermore, plasmonic nanoparticles efficiently convert light into heat [23,24]. Thus, plasmonic nanocomposites are amenable to optically controlled, localized heating. This localized heating is well known in the field of thermoplasmonics, where predominantly dispersed plasmonic nanoparticles and their individual properties or interactions with the living matter have been investigated [25]. The structure-thermoplasmonics relationship manifested in the absorption spectra will also impact the glass-rubber transition and elastic mechanical properties, i.e., the thermomechanical behavior of the polymer nanocomposite films. The latter studies being important for applications of these materials as gas permeation membranes [26,27] are somewhat rare, rendering a predictive power premature.

In this paper, we employ Brillouin light scattering (BLS) as a powerful and nondestructive method to determine the mechanical properties of homogeneous silver-polystyrene (AgPS), one-component hybrid materials with low metal volume fractions. We focus on two major aspects: (i) the influence of the structural control provided by the synthesis of the polymer grafted silver nanoparticles and (ii) the external (global) and plasmonic (local) heating, which entails distinct structural changes. The plasmonic heating contribution constitutes a localized heating effect. This allows creating hot microscopic areas in the bulk film, which are directly probed by BLS. Plasmonic heating is a fast and instantaneous heating effect, owing to the radiative transfer of energy to the metallic nanoparticles. It is, therefore, different from conventional sample heating achieved via convection and conduction in a thermal bath. We complement our investigation with ultraviolet-visible (UV-Vis) spectroscopy, transmission electron microscopy (TEM) tomography, small-angle x-ray scattering (SAXS) measurements, and finite-element method (FEM) simulations to unravel the temperature-induced structural changes.

II. EXPERIMENTAL

A. Materials

The synthesis of the AgPS nanocomposites is described elsewhere [16]. The PS ligands were prepared by reversible addition-fragmentation chain transfer (RAFT) polymerization. The trithiocarbonate end group was transferred into a thiol group by aminolysis. We synthesized ligands with molecular weights of 8, 12, and 18 kg/mol. The Ag nanoparticles were synthesized according to the method by Yamamoto *et al.* [28]: A silver myristate precursor was heated in trimethylamine to 80 °C for 4 h. The obtained Ag nanoparticles were mixed with an excess of PS ligands to achieve a theoretical grafting density of 10 ligands/nm². After that, the mixture was stirred for 65 h. The nanocomposites were purified by three qualitative precipitation steps and a subsequent centrifugation step at the θ condition of the PS ligand. We name our samples PS8k, PS18k, etc. for the respective pure polymer ligand; the Ag nanoparticles grafted with these polymers are termed AgPS8k, AgPS18k, etc., indicating the respective ligand molecular weight.

B. Film preparation and characterization

The films were prepared by spin coating of a 15 wt.% toluene solution on microscope slides with a thickness in the range from 483 to 1598 nm. The films were kept for 10 h in a vacuum oven at 100 °C to remove the residual toluene. The internal structure of the nanocomposite film can be strongly altered using thermal annealing. The as-prepared films were, therefore, subjected to an annealing procedure. Figure S1 in Supplemental Material [29] shows the annealing procedure based on a hot plate. The nanocomposite films were annealed for 1 and 30 min, respectively, on a hot stage with a set temperature of 200 °C. The color of the films changed during the annealing procedure, which can be related to the altered internal structure of the nanocomposite films.

C. Optical spectroscopy

An Analytik Jena SPECORD 250 Plus spectrophotometer was used to measure the UV-Vis spectra.

D. Transmission electron microscopy

Thin films (2.5 wt.% for AgPS18k and 5 wt.% for AgPS8k) were prepared on glass slides with a sacrificial ZnO layer for TEM characterization. Immersion of the coated substrates in a 1 M HCl bath released the nanocomposite film, which floated on the water surface and was subsequently transferred to a TEM grid. The measurements were conducted on a Zeiss EM922 Omega.

E. Electron tomography

For electron tomography analysis, the samples were carbon-sputtered with a Leica EM ACE600 with a thickness of about 3 nm and the TEM grids were cut in half with a razor blade. The samples were measured on a JEOL 2200FS instrument in bright-field mode, operating at an accelerating voltage of 200 kV. Images were taken with a 16-bit 2048×2048 Ultra-Scan 1000XP charge-coupled device camera (Gatan) in a range from $-40°$ to $+40°$ at a $2°$ interval using the GATAN software (version 2.31.734.0). Prealignment of the tilt image series was done with IMOD [30]. After prealignment, videos were compiled using the FIJI open-source software package [31].

F. Small-angle x-ray scattering

For the SAXS measurements, the samples were spin coated on a Kapton® foil, and the measurements were performed at room temperature in a transmission geometry using a Double Ganesha AIR system (SAXSLAB, Denmark). The x-ray source of this laboratory-based system is a rotating copper anode (MicroMax 007HF, Rigaku Corporation, Japan). A position-sensitive detector (PILATUS 300 K, Dectris) recorded the data. To cover the range of scattering vectors q_{SAXS} between 0.03 and $10\,\mathrm{nm}^{-1}$ different detector positions were used with beam sizes between 0.3×0.3 and $0.9 \times 0.9\,\mathrm{mm}^2$. The circularly averaged data were normalized to the incident beam, an assumed sample thickness of 1 mm, and the measurement time before subtraction of the Kapton® foil background. Calculations were done using the software SASFIT (version 0.94.1) written by Kohlbrecher and Bressler [32]. Section S6 of Supplemental Material provides more information about the fit [29].

G. BLS spectroscopy [17]

BLS measurements were performed in a transmission configuration, which allows probing the in-plane, thermally excited phonons in the nanocomposite films along the direction of the scattering wave vector $\mathbf{q} = \mathbf{k_s} - \mathbf{k_i}$, where $\mathbf{k_i}$ and $\mathbf{k_s}$ denote the wave vectors of the incident and scattered photons, respectively. In this configuration, the scattering vector is independent of the sample's refractive index, and can be computed as $q = \sin(\theta/2)4\pi/\lambda$, with θ being the scattering angle and $\lambda = 532$ nm the wavelength of the incident light. The resultant frequency shift of scattered light [in the hypersonic (GHz) region] is resolved by a high-resolution tandem, six-pass Fabry-Pérot interferometer (JRS Instruments). All the results presented were obtained from polarized (VV) BLS measurements. As a result, only longitudinal sound waves are considered. The free spectral range was fixed at 10 GHz by using a mirror spacing of 15 mm. For the temperature scan measurements, the sample temperature was monitored with a platinum resistance detector and adjusted with a homemade temperature controller. At each temperature, the sample was allowed to isothermally equilibrate for 20 min before the spectra were recorded.

H. Differential scanning calorimetry

Differential scanning calorimetry (DSC) measurements were conducted on a TA instruments Discovery DSC 2500 using a heating rate of 20 K/min. Four heating curves were measured. The first run (-40 to $100\,°\mathrm{C}$) cleared the thermal history of the samples without inducing any structural changes and improved the contact between the sample and the pan. The T_g was determined in the second run (-40 to $120\,°\mathrm{C}$). The samples were heated up to $175\,°\mathrm{C}$ in the third run to mimic the thermal annealing steps. The fourth heating curve (-40 to $120\,°\mathrm{C}$) was used to evaluate the T_g of the annealed samples.

I. Thermographic measurements

For thermographic measurements, a VarioCam® HD research 900 IR camera with close-up lens from InfraTec GmbH was used. The camera was mounted in front of the film with an angle of around 60° with respect to the sample plane. The pixel resolution of the IR camera was around $30\,\mu$m at the used working distance. The laser beam ($\lambda = 532$ nm) had an incident angle of around 85°. The laser was focused to a spot size of $90\,\mu$m. Before the measurements, the emissivity of the films was determined using a reference sample with a known emissivity. The power of the incident laser light was varied between 1 and 90 mW. After thermal equilibration of the sample at each laser power, an image of the temperature distribution was taken, from which the maximum temperature was evaluated. This value is the average temperature over an area of $30 \times 30\,\mu\mathrm{m}^2$.

III. RESULTS AND DISCUSSION

A. One-component nanocomposite homogeneous films

Transmission electron microscopy images of drop-cast AgPS8k and AgPS18k [Figs. 1(a) and 1(b)] and a side-view scanning electron microscopy (SEM) image of a spin-cast film [Fig. 1(c)] demonstrate the high uniformity of the individual Ag-polymer ligand nanoparticles and highlight their distribution across the entire polymer nanocomposite film. Also, a TEM tilt series (videos in section S2 of Supplemental Material [29]) demonstrates the homogeneous nanoparticle distribution and lack of clusters. The SAXS intensity patterns confirm the homogeneity and structural control [Fig. 1(e)]. Due to the low contrast of the polystyrene shell, the signal is most sensitive to the silver core of the nanoparticles. At high scattering vectors, q_{SAXS}, the intensity is dominated by the form factor of the particles, whereas at low q_{SAXS} the scattering also refers to the arrangement of the particles, i.e., it is sensitive to the structure factor. Figure 1(e) shows the experimental scattering intensities of the films AgPS8k (blue circles) and AgPS18k (red triangles) along with their corresponding modeling (solid lines): The spheres have a radius of 3.0 nm and a Gaussian particle size distribution with a standard deviation of 0.4 nm. The Percus-Yevick structure factor is based on an effective interaction distance of 6.5 nm and an effective volume fraction of $\phi = 0.35$. For both films, the minimum at $q_{\mathrm{SAXS}} \approx 1.5\,\mathrm{nm}^{-1}$ is attributed to the particle size. Hence, the silver core is well defined and homogeneously distributed all over the film.

The system with the short polymer ligand (AgPS8k) exhibits a Bragg reflection at $q_{\mathrm{SAXS}} \approx 0.5\,\mathrm{nm}^{-1}$, resulting from an effective particle-particle interaction distance of 6.5 nm. For AgPS18k this feature is less pronounced, and the

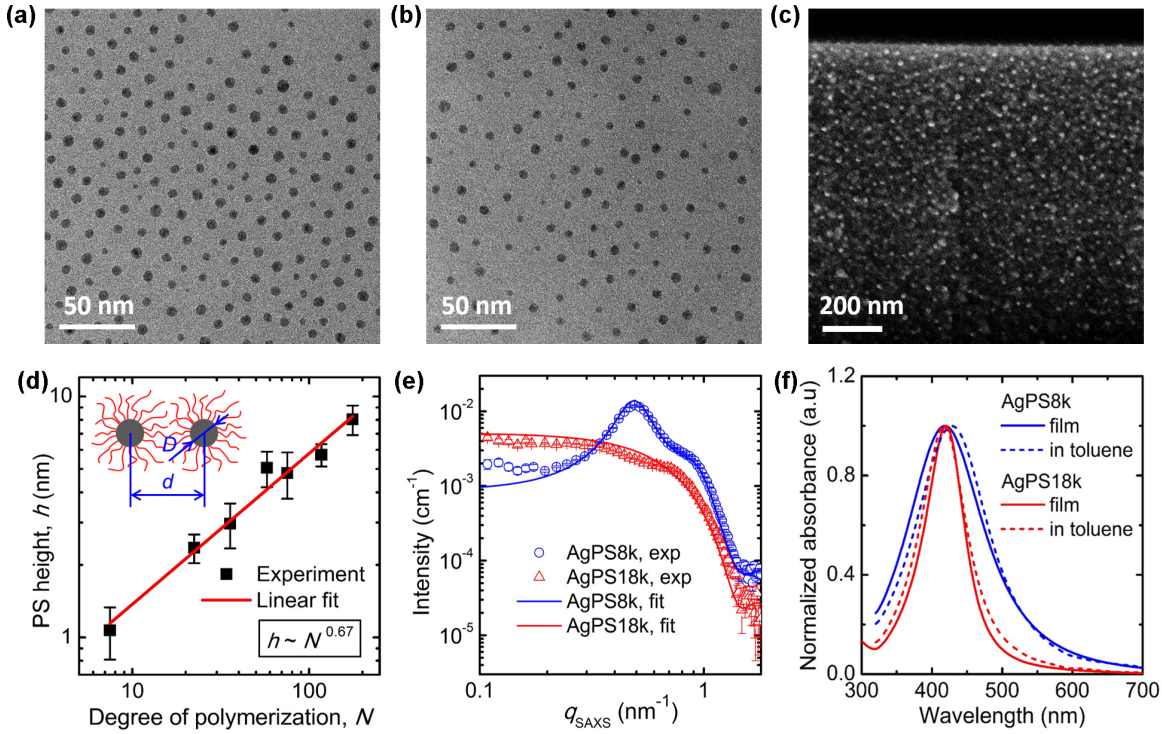

FIG. 1. (a), (b) TEM images of the AgPS8k and AgPS18k samples with silver volume fractions, $\varphi = 0.05$ and 0.014, respectively. (c) SEM image (side view) of an AgPS18k film, where the bright spots indicate the well-dispersed Ag nanoparticles over the whole thickness of the film. (d) The polymer height determined from the TEM images is plotted as a function of the degree of polymerization, which shows a linear relation in the double-logarithmic plot. (e) SAXS patterns of the AgPS8k and AgPS18k films (symbols) and theoretical descriptions (lines; for details, see section S3 in Supplemental Material). (f) UV-Vis spectra of the AgPS8k and AgPS18k samples measured in solid films (solid lines) and toluene (dashed lines).

scattering pattern can be well approximated with a pure form factor. This result gives a hint to the influence of increasing shell thickness to the film morphology: With increasing ligand length, the core-core interaction becomes weaker. According to the Hansen criteria, the structure factor must be >2.85 for crystalline order. In our case, the experimental structure factor has a maximum of 1.5 demonstrating a glasslike order. Overall, the spin coating of the particle-brush dispersion in toluene leads to a homogeneous film. The homogeneity also becomes apparent in the UV-Vis spectra [Fig. 1(f)]. These show a single and well-defined plasmonic peak originating from the individual Ag nanoparticles (NPs) with no discernible aggregation.

The TEM images [Figs. 1(a) and 1(b)] were used to evaluate the interparticle distance d, from which we computed the PS height, $h = (d - D)/2$, where D is the diameter of the Ag nanoparticles. Figure 1(d) depicts h versus degree of polymerization of the grafted PS chains, N, in a double-logarithmic presentation. A scaling relation $h \sim N^{\nu}$ is observed, with the value $\nu = 0.67 \pm 0.05$ exceeding the random coil value (0.5), and implying an extended conformation of the PS chains. Much larger dielectric particle-brush systems also showed a similar scaling exponent [7], which is indicative of high grafting density justifying a brushlike behavior. The interparticle distance in the as-prepared films can be controlled between 2 and 10 nm through the synthesis of densely tethered PS chains. We next examine the elastic properties of the as-prepared films.

The inset to Fig. 2(a) depicts isotropic BLS spectra for the AgPS18k film at three different scattering wave vectors $\mathbf{q}$ at 293 K and low laser power (45 mW), displaying a single acoustic phonon. We will see later that the laser power used here is low enough to leave the speed of sound of the sample unaffected. The linear dispersion in the main plot of Fig. 2(a) shows the acoustic nature of the probed phonons in the AgPS12k and AgPS18k films along with the constituent PS18k film. From the linear dispersions, we calculate the effective medium longitudinal sound velocity as $c_{\mathrm{L,eff}} = 2\pi f/q$, where f is the phonon frequency. The presence of a single acoustic phonon supports the homogeneity of the films on a length scale larger than the probing phonon wavelength range (about 300–800 nm). This homogeneity is consistent with the structures presented in Fig. 1. Counterintuitively, the speed of sound drops with increasing, yet low, volume fraction, φ, of Ag nanoparticles as shown in Fig. 2(b). Applying the Wood's law (section S4 in Supplemental Material [29]), using the density and the longitudinal sound velocity of the individual components fixed to the bulk Ag and PS values, the decrease of $c_{\mathrm{L,eff}}$ with φ can be semiquantitatively represented [solid line in Fig. 2(b)]. The drop of $c_{\mathrm{L,eff}}$ is mainly the result of the considerable density mismatch between Ag and PS, while application of the effective medium presentation assumes good adhesion between the Ag core and PS brush in the glassy state.

Interestingly, Wood's law failed to predict the increase of $c_{\mathrm{L,eff}}(\varphi)$ in a TiO_2 polymer nanocomposite [33], where a soft

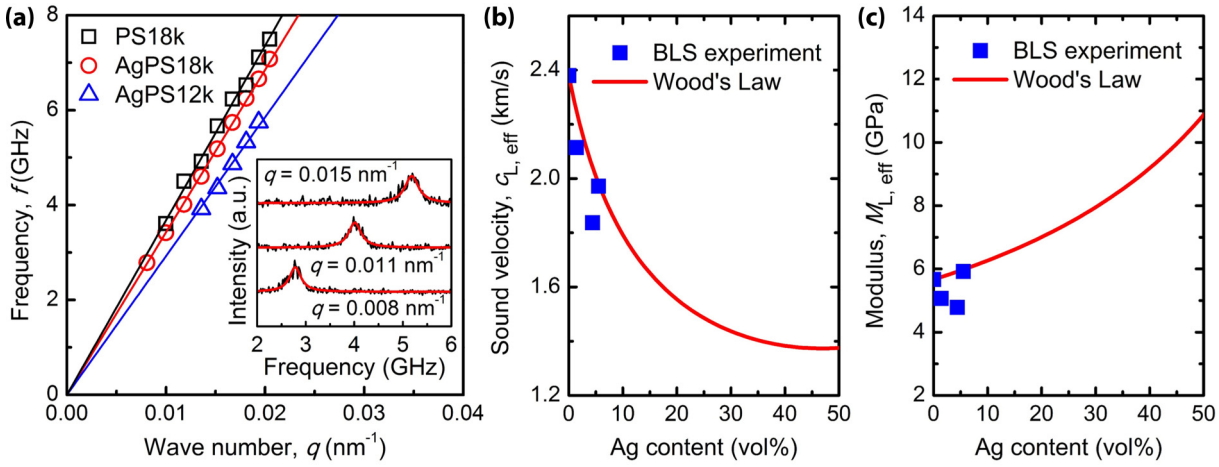

FIG. 2. (a) Linear acoustic dispersion of the longitudinal phonon in the as-prepared AgPS18k and AgPS12k nanocomposite films (red circles and blue triangles), and bulk PS18k (black squares) recorded by BLS. Inset: BLS spectra of a 1.4-μm-thick AgPS18k film, recorded at three different wave numbers using a 532-nm laser at 45 mW, and represented by Lorentzian line shapes (solid red lines). (b) Effective longitudinal sound velocity $c_{\mathrm{L,eff}}$ vs Ag volume fraction. Wood's law representation (red line) was conducted using Eq. (2) in section S4 in Ref. [29] without any adjustable parameter. The densities and sound velocities assume the values of bulk Ag and PS. (c) Computed effective longitudinal modulus of the AgPS nanocomposites in (b) as a function of the Ag volume fraction.

interlayer had to be introduced [34]. The longitudinal elastic modulus, $M_{\mathrm{L,eff}} = \rho_{\mathrm{eff}}\, c^2_{\mathrm{L,eff}}$, an important material property, is shown in Fig. 2(c). Here the effective density, $\rho_{\mathrm{eff}}(\varphi) = \rho_{\mathrm{Ag}}\varphi + \rho_{\mathrm{PS}}(1-\varphi)$ is assumed to be a linear function of the Ag volume fraction using the bulk densities of the two constituents. The Wood's law's prediction (solid red line) with no adjustable parameters is a monotonic increase of $M_{\mathrm{L,eff}}$ with Ag volume fraction. The computed $M_{\mathrm{L,eff}}$ assuming the particular $\rho_{\mathrm{eff}}(\varphi)$ does not capture the observed decrease at low experimental Ag content; an effective lower density for Ag would be needed [33].

The temperature dependence of the modulus is a characteristic feature of hybrid systems that can change their phase state upon heating. In the case of bulk PS film, it is well known that the rate of the decrease of the sound velocity with temperature changes abruptly at the glass-rubber transition as shown for PS18k in Fig. 3 (gray shaded area). The transition occurs about 8 K lower compared to the T_g(∼373 K) obtained from DSC (Supplemental Material, section S5, Fig. S5 [29]). The much lower heating rate can explain this deviation in the BLS experiment [7]. The T_{g} is more accurately defined in the plot of $c_{\mathrm{L,eff}}$ versus $(1/T)$ [35]. For AgPS18k, this transition occurs at a much lower temperature (∼325 K) compared to the DSC data ($T_g = 373$ K). The temperature effect is reversible as indicated by the BLS spectra in the inset of Fig. 3. The discrepancy between the BLS and DSC measurements can be understood by the additional heating effect of the laser light within the focal volume of the laser spot. In the case of AgPS8k ($T_g = 369$ K) with a higher Ag volume fraction than AgPS18k, the even larger disparity of the transition temperature (∼310 K) with the DSC corroborates the notion of laser heating. Given the weak $c_{\mathrm{L,eff}}(T)$ dependence in the glass regime (below T_{g}), the localized heating effect plays a negligible role at 293 K, rendering the composition dependence of the sound velocity in Fig. 2(b) reliable.

Since PS is the majority component, the slopes ${c_{\mathrm{L,eff}}}^{-1}(T = 0\,\mathrm{K})\mathrm{d}c_{\mathrm{L,eff}}/\mathrm{d}T$ in the glassy ($\sim 4 \times 10^{-4}\,\mathrm{K}^{-1}$) and rubbery ($1.4 \times 10^{-3}\,\mathrm{K}^{-1}$) states of the polymer nanocomposites were expectedly found similar to the PS matrix (Table S1 in Ref. [29]); a constant, laser-induced temperature increase ΔT would not significantly impact the values of the PS slopes. The plasmonic origin of the heating is also demonstrated by the very similar transition

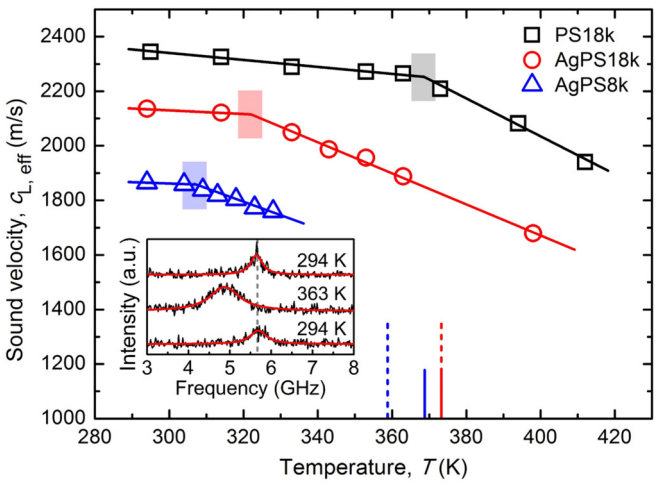

FIG. 3. Longitudinal sound velocities in the as-prepared AgPS18k and AgPS8k nanocomposite films and the bulk PS18k film as a function of temperature. The shaded areas indicate the glass transition temperatures, and the four vertical lines denote the glass transition temperatures obtained from the DSC traces of bulk AgPS18k (solid red), AgPS8k (solid blue), PS18k (dashed red), and PS8k (dashed blue) films. Inset: Anti-Stokes BLS spectra of AgPS18k at three temperatures as indicated in the plot. The BLS spectrum in the lower panel was recorded at the end of the temperature scan after cooling the sample from 363 K back to 294 K. For the AgPS8k and AgPS18k films, the BLS spectra were recorded with laser powers of 45 and 60 mW, respectively.

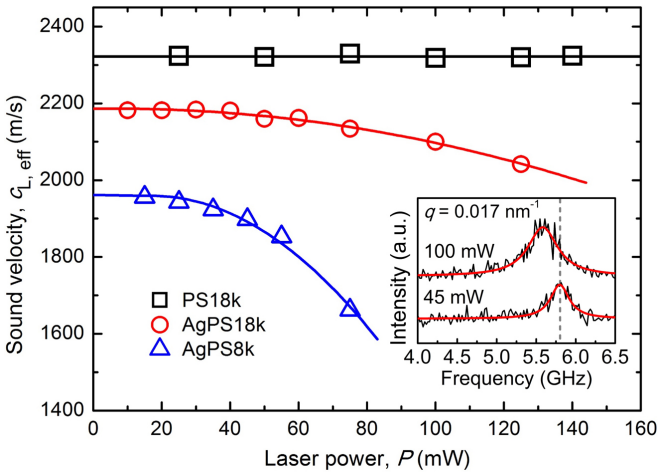

FIG. 4. Effective longitudinal sound velocity in the as-prepared AgPS18k (red circles) and AgPS8k (blue triangles) nanocomposite and PS18k (black squares) films as a function of the laser power at 532 nm. The red and blue solid lines denote a parabolic representation of the experimental sound velocities in AgPS18k and AgPS8k, respectively, whereas the solid black line indicates the power-independent sound velocity in bulk PS18k. Inset: Anti-Stokes BLS spectra at $q = 0.017\,\mathrm{nm}^{-1}$ at laser powers of 45 and 100 mW represented by Lorentzian line shapes.

temperature and temperature dependence of $c_{L,eff}$ in a SiO_2-PS particle-brush film (Fig. S6 in Ref. [29]), where no local laser heating occurs (note Ag nanoparticles induce plasmonic heating, but SiO_2 nanoparticles do not).

To entirely eliminate the laser heating and to have the laser serving as a probe as it is the case for PS (Fig. 3), very low incident light intensities would be necessary. This, however, renders a reliable temperature-dependent study very time-consuming. Instead, we examine next the influence of the local heating on the $c_{L,eff}$ measurement at different laser powers, P. This way we harness the laser source as both a local heater and a probe. For the as-prepared AgPS18k film, the inset to Fig. 4 depicts the BLS redshift when the laser power increases from 45 to 100 mW at an external temperature of 293 K. This is due to the slowdown of $c_{L,eff}$ as a result of the laser-induced local heating. The drop of $c_{L,eff}$ for different laser powers is shown for the as-prepared AgPS8k and AgPS18k films in Fig. 4 and contrasts the expected constant $c_{L,PS}$ in the bulk PS film (squares) due to the absence of light absorption. In the presence of light absorption, the dependence $c_{L,eff}(P)$, shown in Fig. 4, is not linear for both as-prepared nanocomposite films, displaying a stronger dependence on the laser power at high power levels. This relation should also hold for the temperature variation with the laser power due to the linear dependence of $c_{L,eff}$ on temperature. We, therefore, construct $T(P)$ through a combination of $c_{L,eff}(T)$ and $c_{L,eff}(P)$. The former is estimated based on the temperature dependence of the longitudinal speed of sound in bulk PS $c_{L,PS}(T)$ (Fig. 3) and the ratio $\gamma = c_{L,eff}/c_{L,PS}$ at 293 K, i.e., $c_{L,eff}(T) = \gamma c_{L,PS}(T)$ (Fig. S7 in the Supplemental Material [29]).

The relation $T(P)$, depicted in Fig. 5 for AgPS8k and AgPS18k, shows the anticipated (Fig. 4) nonlinear dependency and a change of the slope in the range 360–370 K, corresponding to the T_g's of AgPS8k and AgPS18k. The change of the slope occurs at an external temperature of 293 K because of the local laser heating with an intensity of about $4.4 \times 10^7\,\mathrm{W/m^2}$ (55 mW over a laser spot with a diameter of 40 μm) and $8.0 \times 10^7\,\mathrm{W/m^2}$ (100 mW), respectively. For independent support, we directly measured the laser-power-dependent temperature $T(P)$ using an IR camera. A laser light beam ($\lambda = 532\,\mathrm{nm}$) was focused on the nanocomposite film to a spot with a diameter of 90 μm, and the average temperature in the laser spot at steady state was measured [Fig. 5(b)]. The $T(P)$ diagram from the IR thermometry is in good, semiquantitative agreement with measurements deduced from BLS. Using a correction factor of $P_{IR}(=1.84\,P_{BLS})$ both measurements can be fully overlaid for both nanocomposite films; this factor accounts for the differences in the actual laser power at the focal spot owing to the different laser setups used. The glass-rubber transition is more clearly evident in AgPS18k occurring in the range 90–110 mW and is reversible

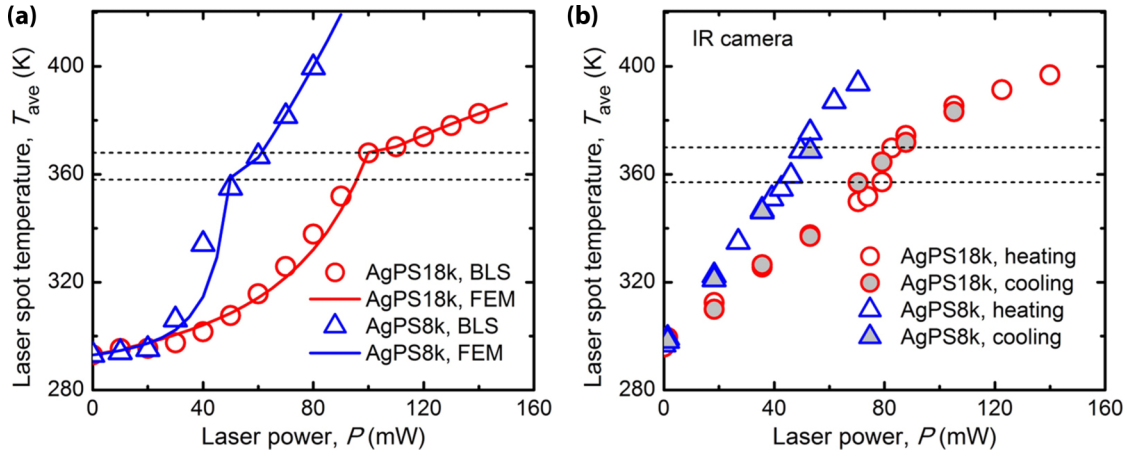

FIG. 5. The local temperature in the laser spot as a function of the laser power in the AgPS18k (red circles) and AgPS8k (blue triangles) films estimated from (a) the data of Fig. 3 and Fig. 4 as described in the text, and (b) using an IR camera. The solid lines indicate the simulation results (Supplemental Material, section S6, Fig. S8 [29]), whereas the horizontal dashed lines indicated the local T_g induced by the laser heating at ambient temperature.

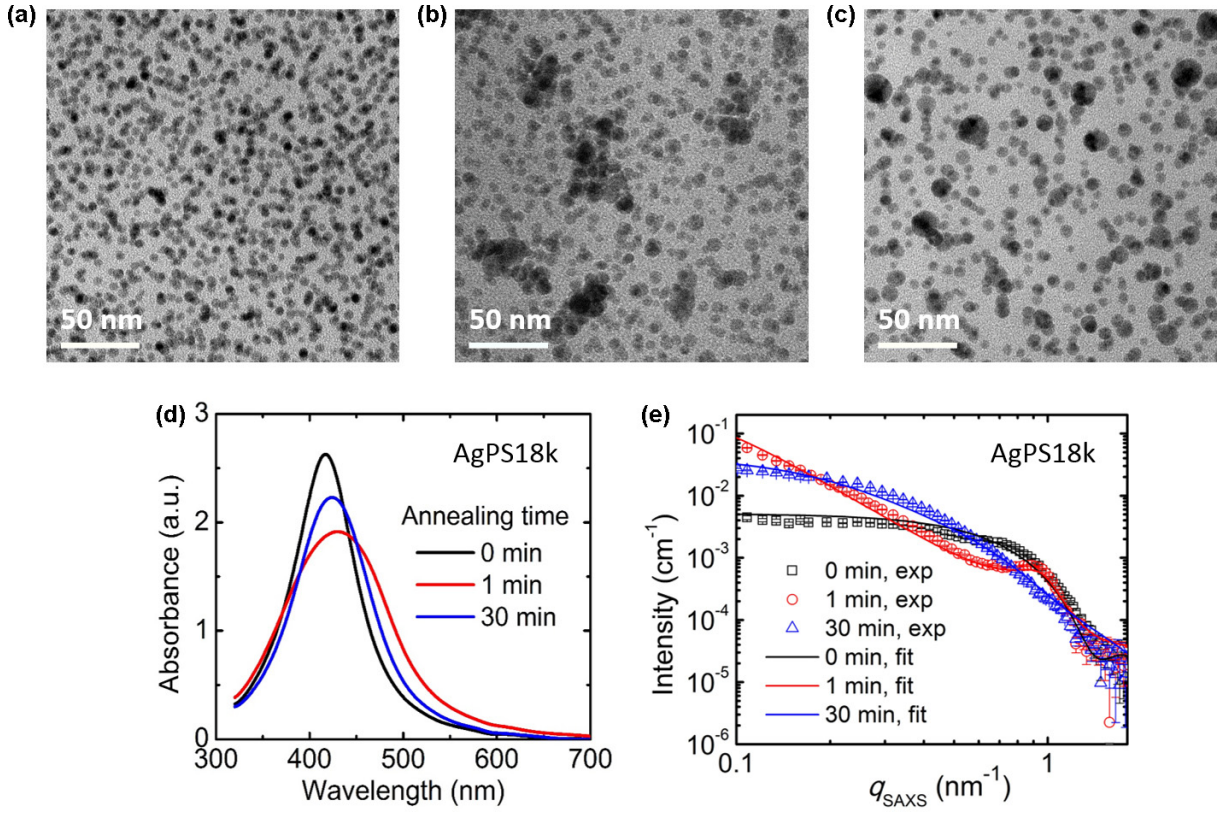

FIG. 6. (a)–(c) TEM images of the AgPS18k films (a) as prepared from spin coating, (b) after 1 min annealing at 200 °C, and (c) after 30 min annealing at 200 °C. (d) UV-Vis and (e) SAXS patterns (symbols) and fits (lines; details in Supplemental Material, section S3 [29]) of the as-prepared and annealed AgPS18k films.

as indicated in the inset of Fig. 3. At higher power and hence in the rubber regime the rate of the temperature increase is reduced.

Figures 5(a) and 5(b) allow for a semiquantitative inspection of the surprisingly low apparent T_g's of the nanocomposite films as shown in Fig. 3; here, 310 K for AgPS8k and 325 K for AgPS18k were recorded with intensities of $3.6 \times 10^7\,\mathrm{W/m^2}$ (45 mW) and $4.8 \times 10^7\,\mathrm{W/m^2}$ (60 mW) (Fig. 3), respectively. Using the laser heating correlation plots of Fig. 5(a) at ambient temperature, the estimated temperature increase is about $\Delta T = 30 \pm 7\,\mathrm{K}$ for AgPS8k at 40 mW and AgPS18k at 60 mW. Assuming a temperature-independent laser heating, the transition temperatures in Fig. 3 should occur at about $T_g - \Delta T$, i.e., at about 330 and 340 K for AgPS8k and AgPS18k, respectively. The overestimation of the transition temperatures (Fig. 3) corroborates the notion of a temperature-dependent laser heating effect. The solid lines in Fig. 5(a) represent simulation results based on a 2D, axis-symmetric model (see Supplemental Material, section S6 and Table S2 for more details [29]) implemented in COMSOL MULTIPHYSICS based on the FEM. By using absorption coefficients linearly dependent on temperature, the $T(P)$ relations obtained from the BLS measurements were successfully captured. We obtained larger absorption coefficients for the AgPS8k film than the AgPS18k film. For both films, the variation of the absorption coefficient with temperature was weaker in the rubbery state than the glassy state.

B. Structural changes induced by thermal annealing

The as-prepared films display homogeneously distributed structures, but the thermodynamic stability is not warranted. Entropic contributions can strongly alter the nanoparticle distribution in composite films as shown recently for AuPS nanoparticles [36]. Thermal treatment also led to significant structural changes in the pure (no additional matrix polymer) nanocomposite films. The structural changes were consistently followed by TEM images, UV-Vis absorption spectra, and SAXS patterns in Fig. 6. Heating well above the T_g of the polymer corona ($T > 423\,\mathrm{K}$) allows the as-prepared film to relax via the speed-up of the translational motion of the untangled PS chains in the nanocomposite film. The randomly dispersed Ag nanoparticles aggregate after annealing for 1 min leading to a local increase of the Ag concentration. The SAXS patterns [Fig. 6(e)] underpin the effect of annealing on the aggregation and dispersion behaviors of the Ag nanoparticles. The AgPS18k sample demonstrates less distinct peaks compared to the AgPS8k sample (both are compared in Fig. S3 in Ref. [29]). Both samples show a qualitatively comparable trend. The intensities obtained after 1 min annealing exhibit the most pronounced forward scattering. Aggregated nanoparticles cause this forward scattering.

The scattering at low q_{SAXS} of the other films (0 and 30 min) is more even, excluding a large number of clusters. The scattering data can be sufficiently well fitted by

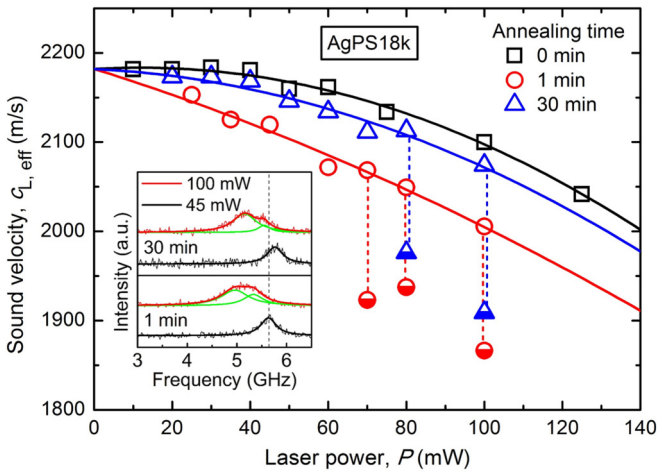

FIG. 7. Effective medium longitudinal sound velocity in annealed AgPS18k nanocomposite films as a function of the laser power, in comparison with the results for the as-prepared AgPS18k film (black squares). The data for the short and long annealing times are indicated by red circles (1 min) and blue triangles (30 min). The half-filled symbols represent the presence of a secondary softer phonon in the BLS spectra. Inset: Anti-Stokes BLS spectra at $q = 0.0167\,\mathrm{nm}^{-1}$ for the AgPS18k films annealed for 1 and 30 min. The spectra at 45 mW (black) and 100 mW (red) are represented by one (black) and two (green) Lorentzian peaks, respectively.

a pure form factor of monodisperse spheres at annealing times of $t = 0\,\mathrm{min}$ ($R = 3.0 \pm 0.4\,\mathrm{nm}$) and $t = 30\,\mathrm{min}$ ($R = 3.0 \pm 0.9\,\mathrm{nm}$). The aggregated structure at $t = 1\,\mathrm{min}$ is a combination of the Percus-Yevick model ($R = 3.0 \pm 0.4\,\mathrm{nm}$, $R_{\mathrm{out}} = 3.3\,\mathrm{nm}$, and $\phi = 0.35$) and clusters ($R_{\mathrm{H}} = 15\,\mathrm{nm}$). The UV-Vis spectra corroborate these structural changes undergoing a redshift and line broadening [Fig. 6(d)]. Surprisingly, prolonged annealing (for 30 min) leads to a redispersion of the nanoparticles and a recovery of the plasmonic resonance spectrum—but at the expense of increased size and polydispersity compared to the as-prepared film [Figs. 6(a) and 6(d)]. These severe structural changes are also confirmed by a TEM tilt series, which highlights the three-dimensional distribution of the Ag nanoparticles (videos in section S2 of Supplemental Material [29]). Furthermore, this unusual aggregation/redispersion phenomenon is universal to Ag-PS corona films. The same effect has also been observed for AgPS6k and AgPS12k films (section S7, Fig. S9 in Ref. [29]). Even longer annealing times exceeding 60 min at $>150\,^{\circ}\mathrm{C}$ lead to Ostwald ripening of the Ag nanoparticles and a further coarsening of the nanostructure. BLS examined the influence of this structural modification on the elastic properties of the nanocomposite films. In particular, the change of the optical resonance spectrum might impact the local heating by the laser light.

Figure 7 presents the BLS-measured sound velocities of two annealed AgPS18k films in comparison with the as-prepared one. The inset depicts the BLS spectra of the two annealed AgPS18k films at two laser powers (45 and 100 mW). In addition to the expected redshift, a second acousticlike phonon peak emerges at high laser powers. In agreement with the structural changes demonstrated in Fig. 6 the $c_{\mathrm{L,eff}}(P)$ of the 30-min annealed film falls between the as-prepared and 1-min annealed ones. For the latter, two phonons are present above 60 mW, whereas for the longer annealed film the second phonon appears at higher powers ($>75\,\mathrm{mW}$). The $c_{\mathrm{L,eff}}(P)$ of the harder phonon in the 30-min annealed film is very similar to the single phonon in the nonannealed film, whereas the 1-min annealed film displays a stronger $c_{\mathrm{L,eff}}(P)$ dependence. We rationalize the correspondence between large nanoparticle clusters and stronger laser heating effects, using qualitative FEM simulations based on a 2D model in COMSOL (detailed information in section S8, Fig. S10, Table S3 in Supplemental Material [29]). The results show that the aggregation of the heat sources lead to higher average temperatures in the surrounding area, which agrees with our experimental findings. This clustering effect on heating is similar to the previously reported, collective heating effect in noble-metal-nanoparticle-based solutions and thermoplasmonic materials [23,37]. The appearance of two phonons at the same acoustic wave number q implies a structural inhomogeneity with length scales larger than the probed phonon wavelength ($\sim 2\pi/q = 500\,\mathrm{nm}$). Figure 6(b), however, suggests much smaller cluster sizes of about 50 nm.

Consequently, it is not clear how the light-induced local heating can lead to a structure coarsening that is responsible for the second soft phonon. Based on Fig. 2(b), its lower sound velocity suggests a higher local Ag composition. For AgPS18k-1-min, with a total volume fraction $\varphi = 0.05$, the local concentration $\varphi = 0.07$ is about 40% higher. Furthermore, this second phonon only becomes measurable at temperatures exceeding the T_{g}, implying the necessity to have some degree of viscoelastic coupling between the nanoparticle clusters. Note that the laser powers used for this measurement are capable of exceeding the T_{g} in the focal volume but are lower than the temperature used for the actual annealing ($200\,^{\circ}\mathrm{C}$).

Consequently, the appearance of the second phonon is a reversible phenomenon. The appearance of a second *softer* phonon is unique to our system. Previous literature reports two longitudinal phonons in a silica poly(2-vinyl pyridine) matrix. Here a *harder* phonon emerged and was justified by solvent selection and annealing-induced microphases where coupling between a percolating silica network was found [38]. The finding of a softer phonon in our case is consistent with the Ag-NP content-dependent $c_{\mathrm{L,eff}}$ discussed in Fig. 2(b). The strong binding of the polymer ligand to the Ag core causes this counterintuitive behavior, which is even robust enough to couple across clusters of AgNPs.

IV. CONCLUSIONS

Homogeneously loaded nanocomposite materials exhibit a wealth of properties, which are still far from being understood. Our contribution bases on dense polymer grafted Ag nanoparticles, where the effective longitudinal speed of sound decreases with increasing Ag content—a counterintuitive finding. The reduction in the speed of sound is, however, analytically captured by Wood's law and is based on the strong binding of the ligand molecule to the AgNP surface. Furthermore, we have been able to show the significant influence of

thermoplasmonic heating on the acoustic and consequently mechanical properties of these nanocomposite samples. The intense local laser heating became apparent when assessing the temperature-dependent $c_{L,\mathrm{eff}}$. Here, an apparent reduction in the glass transition temperature could be explained by the strong heating of the nanocomposite sample in the focal measurement volume. The degree of heating depends on the AgNP concentration and shows a nonlinear behavior. This thermoplasmonic effect can reach local temperatures in excess of the actual glass transition temperature of the hybrid material (∼100 °C of the PS ligand). BLS further elucidated the importance of the overall film morphology. Here, we exploited a particularly unusual behavior of our nanocomposite films: At temperatures much higher than the glass transition temperature (∼200 °C), rapid AgNP clustering sets in. Prolonged annealing at these temperatures led to a redispersion of the clusters at the expense of larger nanoparticles with a higher polydispersity compared to the initial state. This peculiar morphology change was observed consistently in nanocomposites with ligands of various molecular weights. Concomitant to this change in morphology is the appearance of a second, softer phonon mode. This softer mode is only active at local temperatures exceeding the glass transition temperature of the polymer ligand and appears only after the temperature-driven cluster formation. It is indicative of the importance of the local microstructure, in this case, a local increase in AgNP concentration, along with the strong ligand adhesion to the AgNP core. Our paper revealed several unusual properties of well-defined nanocomposite films. Not only did we show how the microstructure itself influences the effective mechanical properties of the nanocomposite film, but we also showed multiple possibilities to influence the longitudinal speed of sound in an (ir)reversible manner by global external and local thermoplasmonic heating.

ACKNOWLEDGMENTS

The authors thank Prof. Dr. André H. Gröschel for electron tomography measurements. P.H. thanks Alexandra Philipp for help with the thermographic measurements. P.H. and M.R. acknowledge the funding by the Lichtenberg Professorship provided by the Volkswagen Foundation. B.G. thanks the Alexander von Humboldt Foundation for the Fellowship. The work was supported by the SFB 840 and DFG Project No. RE3550/2-1 (Bayreuth) and ERC AdG SmartPhon (Grant No. 694977) (Mainz).

The manuscript was written through the contributions of all authors. All authors have approved the final version of the manuscript. P.H. synthesized the polymer nanocomposites and prepared the spin-coated samples. P.H. performed UV/Vis, TEM, DSC, and thermographic measurements. D.S. measured the BLS spectra. Z.W. performed the COMSOL calculations. S.R. performed SAXS measurements and interpretation. All authors discussed the results and jointly wrote the manuscript.

The authors declare no competing financial interest.

[1] D. K. Avasthi, Y. K. Mishra, D. Kabiraj, N. P. Lalla, and J. C. Pivin, Nanotechnology **18**, 125604 (2007).
[2] L. Balan and D. Burget, Eur. Polym. J. **42**, 3180 (2006).
[3] V. Torrisi and F. Ruffino, Coatings **5**, 378 (2015).
[4] X. Y. Huang, P. K. Jiang, and L. Y. Xie, Appl. Phys. Lett. **95**, 242901 (2009).
[5] X. Li, W. Park, Y. P. Chen, and X. Ruan, J. Heat Transfer **139**, 022401 (2016).
[6] C. A. Grabowski, H. Koerner, J. S. Meth, A. Dang, C. M. Hui, K. Matyjaszewski, M. R. Bockstaller, M. F. Durstock, and R. A. Vaia, ACS Appl. Mater. Interfaces **6**, 21500 (2014).
[7] Y. Cang, A. N. Reuss, J. Lee, J. Yan, J. Zhang, E. Alonso-Redondo, R. Sainidou, P. Rembert, K. Matyjaszewski, M. R. Bockstaller, and G. Fytas, Macromolecules **50**, 8658 (2017).
[8] W. L. Ong, S. Majumdar, J. A. Malen, and A. J. H. McGaughey, J. Phys. Chem. C **118**, 7288 (2014).
[9] W. L. Ong, S. M. Rupich, D. V. Talapin, A. J. McGaughey, and J. A. Malen, Nat. Mater. **12**, 410 (2013).
[10] S. Li, M. Meng Lin, M. S. Toprak, D. K. Kim, and M. Muhammed, Nano Rev. **1**, 5214 (2010).
[11] X. Bouju, E. Duguet, F. Gauffre, C. R. Henry, M. L. Kahn, P. Melinon, and S. Ravaine, Adv. Mater. **30**, 1706558 (2018).
[12] P. Akcora, H. Liu, S. K. Kumar, J. Moll, Y. Li, B. C. Benicewicz, L. S. Schadler, D. Acehan, A. Z. Panagiotopoulos, V. Pryamitsyn, V. Ganesan, J. Ilavsky, P. Thiyagarajan, R. H. Colby, and J. F. Douglas, Nat. Mater. **8**, 354 (2009).
[13] S. Fischer, A. Salcher, A. Kornowski, H. Weller, and S. Forster, Angew. Chem. Int. Ed. **50**, 7811 (2011).
[14] D. Dukes, Y. Li, S. Lewis, B. Benicewicz, L. Schadler, and S. K. Kumar, Macromolecules **43**, 1564 (2010).
[15] S. Ehlert, C. Stegelmeier, D. Pirner, and S. Forster, Macromolecules **48**, 5323 (2015).
[16] P. Hummel, A. Lerch, S. M. Goller, M. Karg, and M. Retsch, Polymers **9**, 659 (2017).
[17] E. Alonso-Redondo, M. Schmitt, Z. Urbach, C. M. Hui, R. Sainidou, P. Rembert, K. Matyjaszewski, M. R. Bockstaller, and G. Fytas, Nat. Commun. **6**, 8309 (2015).
[18] S. Ehlert, S. M. Taheri, D. Pirner, M. Drechsler, H. W. Schmidt, and S. Forster, ACS Nano **8**, 6114 (2014).
[19] S. A. Kim, R. Mangal, and L. A. Archer, Macromolecules **48**, 6280 (2015).
[20] W. Lewandowski, M. Fruhnert, J. Mieczkowski, C. Rockstuhl, and E. Gorecka, Nat. Commun. **6**, 6590 (2015).
[21] K. Volk, J. P. S. Fitzgerald, P. Ruckdeschel, M. Retsch, T. A. F. König, and M. Karg, Adv. Opt. Mater. **5**, 1600971 (2017).
[22] K. Volk, J. P. Fitzgerald, M. Retsch, and M. Karg, Adv. Mater. **27**, 7332 (2015).
[23] H. H. Richardson, M. T. Carlson, P. J. Tandler, P. Hernandez, and A. O. Govorov, Nano Lett. **9**, 1139 (2009).
[24] O. Neumann, A. S. Urban, J. Day, S. Lal, P. Nordlander, and N. J. Halas, ACS Nano **7**, 42 (2013).
[25] G. Baffou and R. Quidant, Laser Photonics Rev. **7**, 171 (2013).
[26] T. C. Merkel, B. D. Freeman, R. J. Spontak, Z. He, I. Pinnau, P. Meakin, and A. J. Hill, Science **296**, 519 (2002).
[27] C. R. Bilchak, E. Buenning, M. Asai, K. Zhang, C. J. Duming, S. K. Kumar, Y. C. Huang, B. C. Benicewicz, D. W. Gidley,

S. W. Cheng, A. P. Sokolov, M. Minelli, and F. Doghieri, Macromolecules **50**, 7111 (2017).

[28] M. Yamamoto, Y. Kashiwagi, and M. Nakamoto, Langmuir **22**, 8581 (2006).

[29] See Supplemental Material at http://link.aps.org/supplemental/10.1103/PhysRevMaterials.2.123605 for a schematic of the annealing procedure, details of the effective medium analysis, further investigations of the glass transition temperature of the samples, SAXS characterizations of the samples, the annealing effect on the samples' morphology, COMSOL simulation results of the particles' collective heating effect on the laser spot temperature, and a video on the electron tomography tilt series.

[30] J. R. Kremer, D. N. Mastronarde, and J. R. McIntosh, J. Struct. Biol. **116**, 71 (1996).

[31] J. Schindelin, I. Arganda-Carreras, E. Frise, V. Kaynig, M. Longair, T. Pietzsch, S. Preibisch, C. Rueden, S. Saalfeld, B. Schmid, J. Y. Tinevez, D. J. White, V. Hartenstein, K. Eliceiri, P. Tomancak, and A. Cardona, Nat. Methods **9**, 676 (2012).

[32] I. Bressler, J. Kohlbrecher, and A. F. Thunemann, J. Appl. Crystallogr. **48**, 1587 (2015).

[33] E. Schechtel, Y. Yan, X. Xu, Y. Cang, W. Tremel, Z. Wang, B. Li, and G. Fytas, J. Phys. Chem. C **121**, 25568 (2017).

[34] S. Cheng, V. Bocharova, A. Belianinov, S. Xiong, A. Kisliuk, S. Somnath, A. P. Holt, O. S. Ovchinnikova, S. Jesse, H. Martin, T. Etampawala, M. Dadmun, and A. P. Sokolov, Nano Lett. **16**, 3630 (2016).

[35] S. Mirigian and K. S. Schweizer, J. Chem. Phys. **140**, 194507 (2014).

[36] R. Zhang, B. Lee, C. M. Stafford, J. F. Douglas, A. V. Dobrynin, M. R. Bockstaller, and A. Karim, Proc. Natl. Acad. Sci. USA **114**, 2462 (2017).

[37] G. Baffou, R. Quidant, and C. Girard, Phys. Rev. B **82**, 165424 (2010).

[38] D. Zhao, D. Schneider, G. Fytas, and S. K. Kumar, ACS Nano **8**, 8163 (2014).